Super Resolution of Multispectral Images using $\ell 1$ Image Models and interband correlations

Miguel Vega · Javier Mateos · Rafael Molina · Aggelos K. Katsaggelos

Abstract In this paper we propose a novel super-resolution based algorithm for the pansharpening of multispectral images. Within the Bayesian formulation, the proposed methodology incorporates prior knowledge on the expected characteristics of multispectral images; that is, it imposes smoothness within each band by means of the energy associated with the $\ell 1$ norm of vertical and horizontal first order differences of image pixel values and also takes into account the correlation among the bands of the multispectral image. The observation process is modeled using the sensor characteristics of both panchromatic and multispectral images. The method is tested on real and synthetic images, compared with other pansharpening methods, and the quality of the results assessed both qualitatively and quantitatively.

Keywords Pansharpening · super-resolution · multispectral images · Bayesian approach · variational methods · $\ell 1$ image models · interband correlations

M. Vega
Dept. de Lenguajes y Sistemas Informáticos,
Universidad de Granada, 18071 Granada, Spain
E-mail: mvega@ugr.es

J. Mateos · R. Molina
Dept. de Ciencias de la Computación e I. A.
Universidad de Granada, 18071 Granada, Spain

A.K. Katsaggelos
Dept. of Electrical Engineering and Computer Science,
Northwestern University, Evanston, Illinois 60208-3118

1 Introduction

Nowadays most remote sensing systems include sensors able to capture, simultaneously, several low spatial resolution images of the same area on different wavelengths, forming a multispectral image, along with a high spatial resolution panchromatic image, a single band image covering a wide spectral range. The main advantage of the multispectral image over the panchromatic one is that it allows for a better land type and use recognition. However, due to its lower spatial resolution, information on the objects shape and texture may be lost. In contrast, the panchromatic image allows for a better recognition of the objects in the scene and their textures but provides no information about their spectral properties.

Super resolution of multispectral images, also called pansharpening, is an approach that jointly processes the multispectral and panchromatic images in order to obtain a new multispectral image that, ideally, exhibits the spectral characteristics of the observed multispectral image and the spatial resolution of the panchromatic one. A number of pansharpening methods have been proposed in the literature following different approaches. Nuñez *et al.* [12] and Otazu *et al.*[13] used a wavelet decomposition of the panchromatic image to add the details of the panchromatic image, either to each band of the multispectral image, or to an intensity image obtained from the multispectral image. Based on the same principle, the contourlet transform has been used in [10] and this transform was combined with principal component analysis in [15]. Another multiresolution approach, using the generalized Laplacian pyramid, was presented in [2] in which the high-pass details of the panchromatic image are weighted locally before being injected into the resampled multispectral bands.

Khan *et al.* [7] proposed to add, to the upsampled multispectral bands, the details from the panchromatic image weighted by a factor calculated to minimize a complex index that takes into account the change in mean and variance of the multispectral bands as well as the correlation of the panchromatic image and each multispectral band. Price [14] formulated the relationship between the panchromatic and multispectral images and estimated each pixel of the pansharpened image from the panchromatic and multispectral values weighted by a value obtained from a 3×3 array of low-resolution data values centered on each low-resolution pixel. Recently, super-resolution techniques have also been applied to the pansharpening problem [11] with improved results. Such approaches model the relationship between the panchromatic and multispectral images, similarly to the Price method, but also impose restrictions on the reconstruction process to control noise and provide more natural, distortion free, images. A description of classical approaches can be found in [17] and a comparison of some algorithms for pansharpening was carried out in [3].

In this paper we propose a super-resolution based pansharpening approach, within the Bayesian formulation. It uses an image model which imposes smoothness over each band of the pansharpened multispectral image by mean of the $\ell 1$ norm of vertical and horizontal first order differences of image pixel values and takes into account the correlation among the bands of the multispectral image. Note that some authors have considered the correlation between the multispectral bands and the panchromatic image (see [7] for instance) to control the amount of information to be injected from the panchromatic image into the multispectral high resolution image by the pansharpening process. However, the approach we propose here is different since we are considering the correlation between the multispectral bands themselves, that is, the similarity of a pixel to those located at the same position in the other bands. To the best of our knowledge, this is the first time that this correlation is explicitly incorporated into the modeling of the pansharpening problem. Notice also that one of the weakness of many pansharpening methods is that they introduce detail information from the panchromatic image in bands that are not covered by this panchromatic image. Other methods, see for instance [13, 11, 7], introduce details depending on factors as the correlation between the panchromatic image and the multispectral band or the relative spectral response of the panchromatic and multispectral sensors. However, these methods may not successfully pansharpen spectral bands that are only partially covered by the panchromatic image. By taking into account the correlation among the different spectral bands, the proposed method will better pansharpen in spectral bands that are partially covered by the panchromatic image.

The paper is organized as follows. In section 2 the Bayesian modeling and inference for super-resolution reconstruction of multispectral images is presented. Section 3 describes the variational approximation of the posterior distribution of the high spatial resolution multispectral image and how inference is performed. Section 4 presents experimental results and section 5 concludes the paper.

2 Bayesian Modeling and Inference

Let us assume that $\mathbf{y}$, the unknown high spatial resolution multispectral image we would have observed under ideal conditions, has B bands $\mathbf{y}_b$, $b = 1, \ldots, B$, each with m rows and n columns, that is, $\mathbf{y} = [\mathbf{y}_1^t, \mathbf{y}_2^t, \ldots, \mathbf{y}_B^t]^t$, where each band of this image is expressed as a $p \times 1$ column vector, with $p = m \times n$, by lexicographically ordering the pixels in the band, and t denotes the transpose of a vector or matrix.

The observed low spatial resolution multispectral image $\mathbf{Y}$, that is, the multispectral image captured by the sensor, has B bands $\mathbf{Y}_b$, $b = 1, \ldots, B$, each one of M rows by N columns, with $M < m$ and $N < n$. For instance, in LandSat 7 ETM+ imaginery (`http://landsat.gsfc.nasa.gov/`) the multispectral sensor provides a multispectral image with six bands (three bands in the visible spectrum plus three bands in the infrared) with a spatial resolution of 30 meters per pixel, plus a thermal band with a spatial resolution of 60 meters per pixel. These bands are also stacked into the vector $\mathbf{Y} = [\mathbf{Y}_1^t, \mathbf{Y}_2^t, \ldots, \mathbf{Y}_B^t]^t$, where each band of this image is also expressed as a $P \times 1$ column vector, $P = M \times N$, by lexicographically ordering the pixels in the band.

The sensor also provides us with a panchromatic image $\mathbf{x}$ of size $p = m \times n$, a single band image that covers a wide spectral area. In the case of a Landsat 7 ETM+ image, the panchromatic image, with a spatial resolution of 15 meters per pixel, covers a large zone on the visible spectrum and the near infrared. Figure 1 shows the spectral response covered by the observed low spatial resolution and panchromatic Landsat 7 ETM+ bands (except the thermal band). While the multispectral image is able to capture the spectral information of the scene, the panchromatic image does not provide spectral information but its spatial resolution is higher than that of the multispectral image.

The objective of the super-resolution reconstruction of multispectral images is to obtain an estimate of the
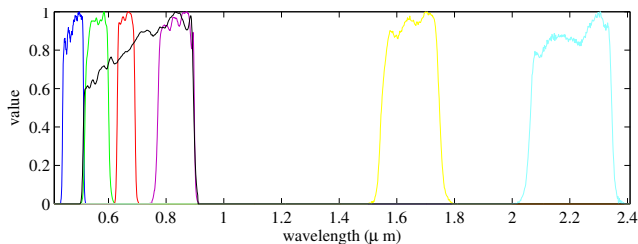
Fig. 1 Landsat 7 ETM+ band spectral responses normalized to one. Curve in black represents the response of the panchromatic sensor.

unknown high spatial resolution multispectral image $\mathbf{y}$ given the panchromatic high spatial resolution observation $\mathbf{x}$ and the low spatial resolution multispectral observation $\mathbf{Y}$.

The Bayesian formulation of this problem requires the definition of the joint distribution of the high spatial resolution multispectral, the low spatial resolution multispectral and panchromatic images, $p(\mathbf{y}, \mathbf{Y}, \mathbf{x})$. This joint distribution is defined as

$$p(\mathbf{y}, \mathbf{Y}, \mathbf{x}) = p(\mathbf{y})p(\mathbf{Y}, \mathbf{x}|\mathbf{y}). \tag{1}$$

Inference is based on the distribution $p(\mathbf{y}|\mathbf{Y}, \mathbf{x})$. Let us now describe those probability distributions.

2.1 Image prior model

In this paper we propose a prior model based on the $\ell 1$ norm [16] to take into account the smoothness within each band plus an auto-regressive model to exploit the correlation among image bands. Thus, we propose the multispectral image prior

$$p(\mathbf{y}) \propto c(\mathbf{y}) \prod_{b=1}^{B} s(\mathbf{y}_b). \tag{2}$$

The smoothness within each multispectral band is modeled by the terms, $s(\mathbf{y}_b)$, $b = 1, ..., B$, which are $\ell 1$ based priors defined as

$$s(\mathbf{y}_b) = \exp\left\{ -\sum_{i=1}^{p} \left[\alpha_b^h \| \Delta_i^h(\mathbf{y}_b) \|_1 + \alpha_b^v \| \Delta_i^v(\mathbf{y}_b) \|_1 \right] \right\}, \tag{3}$$

where $\Delta_i^h(\mathbf{y}_b)$ and $\Delta_i^v(\mathbf{y}_b)$ represent the horizontal and vertical first order differences at pixel i, respectively, and α_b^h and α_b^v are the horizontal and vertical model parameters of the band b. The idea behind this model is to consider the image as a set of relatively smooth objects or regions separated by strong edges. This knowledge is common in practically all the satellite and natural images. This model enforces smoothness within the objects in each image band while preserving their edges.

The term $c(\mathbf{y})$, which takes into account the correlations among different high resolution bands, is given by

$$c(\mathbf{y}) = \exp\left\{ -\sum_{b=1}^{B} \sum_{b'>b}^{B} \frac{\nu_{bb'}}{2} \| \mathbf{y}_b - \mathbf{y}_{b'} \|^2 \right\}, \tag{4}$$

with $\nu_{bb'} \geq 0$ for $b' > b$, thus enforcing similarity among the pixels at the same position in the different bands, where $\{\nu_{bb'}\}$ are the parameters that control the similarity between band b and band b'. Note that this prior assumes that the contents of the bands are similar, that is, each spectral band is rather narrow and the center frequencies of such bands are not very far apart. This is true in most multispectral imaging systems. Of course, as the wavelengths of the bands become more different, the difference in the content of the bands will increase and their correlation will decrease. This situation is handled well by our model, since it allows for setting a high value of $\nu_{bb'}$ for bands b and b' with a high correlation and a value of $\nu_{bb'}$ close or equal to zero for bands b and b' without similar values for pixels at the same position. Note that different spectral bands may have different range of values and different energy, either because of the contribution of the real scene to that specific band or because they have been captured with different gains. In this case, this prior will introduce flux variations in the bands which is an undesirable effect since it modifies the spectral signature of the objects in the scene. In order to maintain the flux in each band and, hence, preserve the spectral properties of the multispectral image, prior to any processing we normalize the flux in each band to one so all the bands have equal flux. After pansharpening we rescale the flux in each band.

2.2 Degradation model

Since the observed panchromatic and low resolution multispectral images are independent given the real high resolution multispectral image to be estimated, we can write

$$p(\mathbf{Y}, \mathbf{x}|\mathbf{y}) = p(\mathbf{Y}|\mathbf{y})p(\mathbf{x}|\mathbf{y}). \tag{5}$$

For each low resolution multispectral image band, we consider the model

$$\mathbf{Y}_b = \mathbf{H}\mathbf{y}_b + \mathbf{n}_b, b = 1, \dots, B,$$

where the degradation matrix $\mathbf{H}$ can be written as $\mathbf{H} = \mathbf{DB}$, with $\mathbf{B}$ a $p \times p$ blurring matrix which takes into account the sensor integration function and any other blur that may degrade the image and $\mathbf{D}$ a $P \times p$ decimation operator, and $\mathbf{n}_b$ the noise term assumed to

be independent white Gaussian of known variance β_b^{-1}. The conditional distribution of the observed image $\mathbf{Y}$ given $\mathbf{y}$ is given by

$$p(\mathbf{Y}|\mathbf{y}) = \prod_{b=1}^{B} p(\mathbf{Y}_b|\mathbf{y}_b)$$

$$\propto \prod_{b=1}^{B} \exp\left\{-\frac{1}{2}\beta_b \parallel \mathbf{Y}_b - \mathbf{H}\mathbf{y}_b \parallel^2\right\}. \qquad (6)$$

The panchromatic image $\mathbf{x}$ is modeled as [11]

$$\mathbf{x} = \sum_{b=1}^{B} \lambda_b \mathbf{y}_b + \mathbf{v}, \qquad (7)$$

where $\lambda_b \geq 0$, $b = 1, 2, \ldots, B$, are known quantities that can be obtained from the sensor spectral characteristics, and $\mathbf{v}$ is the capture noise that is assumed to be Gaussian with zero mean and known variance γ^{-1}. The role of λ_b, $b = 1, 2, \ldots, B$, is to weight the contribution of each high spatial resolution multispectral band $\mathbf{y}_b$ to the panchromatic image. The values can be calculated, as we will see later, from the spectral response of the sensor. Note that if any of the bands of the multispectral image is not covered by the panchromatic image, its contribution will be zero. Note also that the incorporation of the sensor spectral response has also been applied to other methods such as the wavelet based method called Wisper [13]. Based on this model, the distribution of the panchromatic image $\mathbf{x}$ given $\mathbf{y}$, is given by

$$p(\mathbf{x}|\mathbf{y}) \propto \exp\left\{-\frac{1}{2}\gamma \parallel \mathbf{x} - \sum_{b=1}^{B} \lambda_b \mathbf{y}_b \parallel^2\right\}. \qquad (8)$$

3 Bayesian Inference and Variational Approximation of the Posterior Distribution

In this paper we assume that all model parameters are known or previously estimated. Then, the Bayesian paradigm dictates that inference on $\mathbf{y}$ should be based on

$$p(\mathbf{y}|\mathbf{Y}, \mathbf{x}) = \frac{p(\mathbf{y}, \mathbf{Y}, \mathbf{x})}{p(\mathbf{Y}, \mathbf{x})} = \frac{p(\mathbf{y})p(\mathbf{Y}, \mathbf{x}|\mathbf{y})}{p(\mathbf{Y}, \mathbf{x})},$$

where $p(\mathbf{y}, \mathbf{Y}, \mathbf{x})$ has been defined in Eq. (1), and $p(\mathbf{y})$, $p(\mathbf{Y}, \mathbf{x}|\mathbf{y})$ have been defined in Eqs. (2) and (5), respectively.

Since $p(\mathbf{y}|\mathbf{Y}, \mathbf{x})$ can not be found in closed form, we apply variational methods to approximate this distribution by a distribution $q(\mathbf{y})$. The variational criterion used to find $q(\mathbf{y})$ is the minimization of the Kullback-Leibler (KL) divergence, given by [8]

$$C_{KL}(q(\mathbf{y})\|p(\mathbf{y}|\mathbf{Y}, \mathbf{x}))$$

$$= \int q(\mathbf{y}) \log\left(\frac{q(\mathbf{y})}{p(\mathbf{y}|\mathbf{Y}, \mathbf{x})}\right) d\mathbf{y}$$

$$= \int q(\mathbf{y}) \log\left(\frac{q(\mathbf{y})}{p(\mathbf{y}, \mathbf{Y}, \mathbf{x})}\right) d\mathbf{y} + \text{const}$$

$$= \mathcal{M}(q(\mathbf{y}), \mathbf{Y}, \mathbf{x}) + \text{const}, \qquad (9)$$

which is always non negative and equal to zero only when $q(\mathbf{y}) = p(\mathbf{y}|\mathbf{Y}, \mathbf{x})$.

Unfortunately, due to the form of the $\ell 1$ prior, the above integral can not be evaluated. However, we can rewrite $s(\mathbf{y}_b)$ in Eq. (3) in the more convenient form as

$$s(\mathbf{y}_b) = \exp\left\{-\sum_{i=1}^{p}\left[\alpha_b^h \sqrt{(\Delta_i^h(\mathbf{y}_b))^2}\right]\right.$$
$$\left. - \sum_{i=1}^{p}\left[\alpha_b^v \sqrt{(\Delta_i^v(\mathbf{y}_b))^2}\right]\right\}, \qquad (10)$$

where the $\ell 1$ norm can be majorized by a function which renders the integral easier to calculate.

Let us consider the following inequality, also used in [4], which states that, for any $w \geq 0$ and $z > 0$

$$\sqrt{w} \leq \frac{w + z}{2\sqrt{z}}. \qquad (11)$$

Using this inequality in Eq. (10), we define the functional

$$M(\mathbf{y}_b, \mathbf{u}_b^h, \mathbf{u}_b^v) = \exp\left\{-\sum_{i=1}^{p}\left[\alpha_b^h \frac{(\Delta_i^h(\mathbf{y}_b))^2 + \mathbf{u}_b^h(i)}{2\sqrt{\mathbf{u}_b^h(i)}}\right]\right.$$
$$\left. - \sum_{i=1}^{p}\left[\alpha_b^v \frac{(\Delta_i^v(\mathbf{y}_b))^2 + \mathbf{u}_b^v(i)}{2\sqrt{\mathbf{u}_b^v(i)}}\right]\right\}, \qquad (12)$$

where we used $w = (\Delta_i^h(\mathbf{y}_b))^2$ or $w = (\Delta_i^v(\mathbf{y}_b))^2$ and $z = \mathbf{u}_b^h(i)$ or $z = \mathbf{u}_b^v(i)$, depending on the direction h or v we are considering, where $\mathbf{u}_b^h \in (R^+)^p$, $\mathbf{u}_b^v \in (R^+)^p$ are p-dimensional vectors with components $\mathbf{u}_b^h(i)$ and $\mathbf{u}_b^v(i)$, $i = 1, \ldots, p$, that need to be computed and have, as will be shown later, an intuitive interpretation related to the unknown images $\mathbf{y}_b$.

Comparing Eq. (12) to Eq. (10), we obtain

$$s(\mathbf{y}_b) \geq \text{const} \cdot M(\mathbf{y}_b, \mathbf{u}_b^h, \mathbf{u}_b^v).$$

This leads to the following lower bound for the joint probability distribution

$$p(\mathbf{y}, \mathbf{Y}, \mathbf{x}) \geq \text{const} \cdot p(\mathbf{Y}|\mathbf{y})p(\mathbf{x}|\mathbf{y})c(\mathbf{y}) \prod_{b=1}^{B} M(\mathbf{y}_b, \mathbf{u}_b^h, \mathbf{u}_b^v)$$

$$= F(\mathbf{y}, \mathbf{Y}, \mathbf{x}, \mathbf{u}^h, \mathbf{u}^v), \qquad (13)$$

where $\mathbf{u}^d = [\mathbf{u}_1^{d^t}, \mathbf{u}_2^{d^t}, \ldots, \mathbf{u}_B^{d^t}]^t$ for $d = h, v$.

Hence, by defining

$$\tilde{\mathcal{M}}(q(\mathbf{y}), \mathbf{Y}, \mathbf{x}, \mathbf{u}^h, \mathbf{u}^v) =$$
$$\int q(\mathbf{y}) \log\left(\frac{q(\mathbf{y})}{F(\mathbf{y}, \mathbf{Y}, \mathbf{x}, \mathbf{u}^h, \mathbf{u}^v)}\right) d\mathbf{y},$$

and using Eq. (13), we obtain

$$\mathcal{M}(\mathbf{q}(\mathbf{y}), \mathbf{Y}, \mathbf{x}) \le \min_{\mathbf{u}^h, \mathbf{u}^v} \tilde{\mathcal{M}}(\mathbf{q}(\mathbf{y}), \mathbf{Y}, \mathbf{x}, \mathbf{u}^h, \mathbf{u}^v),$$

where $\mathcal{M}(\mathbf{q}(\mathbf{y}), \mathbf{Y}, \mathbf{x})$ was defined in Eq. (9).

Therefore, by finding a sequence of distributions $\{\mathbf{q}^k(\mathbf{y})\}$, $k = 1, 2, \ldots$, that monotonically decreases the functional $\tilde{\mathcal{M}}(\mathbf{q}(\mathbf{y}), \mathbf{Y}, \mathbf{x}, \mathbf{u}^h, \mathbf{u}^v)$ for fixed $\mathbf{u}^h$ and $\mathbf{u}^v$, we also obtain a sequence of an ever decreasing upper bound of $C_{KL}(\mathbf{q}(\mathbf{y})\|\mathbf{p}(\mathbf{y}|\mathbf{Y}, \mathbf{x}))$ due to Eq. (9). Even more, minimizing $\tilde{\mathcal{M}}(\mathbf{q}(\mathbf{y}), \mathbf{Y}, \mathbf{x}, \mathbf{u}^h, \mathbf{u}^v)$ with respect to $\mathbf{u}^h$ and $\mathbf{u}^v$, also generates vector sequences $\{\mathbf{u}^{h^k}\}$ and $\{\mathbf{u}^{v^k}\}$ that tighten the upper-bound for each distribution $\mathbf{q}^k(\mathbf{y})$. Therefore, the sequence $\{\mathbf{q}^k(\mathbf{y})\}$ is coupled with the sequences $\{\mathbf{u}^{h^k}\}$ and $\{\mathbf{u}^{v^k}\}$. We develop the following iterative algorithm to find such sequences. We note that the process to find the best posterior distribution approximation of the image in combination with $\mathbf{u}^h$ and $\mathbf{u}^v$ is a very natural extension of the Majorization-Minimization approach to function optimization [9].

Algorithm 1 *Posterior image distribution estimation.*

Given $\mathbf{u}^{h^1} \in (R^+)^{Bp}$ *and* $\mathbf{u}^{v^1} \in (R^+)^{Bp}$;
for $k = 1, 2, \ldots$ *until a stopping criterion is met:*

1. Find

$$\mathbf{q}^k(\mathbf{y}) = \arg\min_{\mathbf{q}(\mathbf{y})} \tilde{\mathcal{M}}(\mathbf{q}(\mathbf{y}), \mathbf{Y}, \mathbf{x}, \mathbf{u}^{h^k}, \mathbf{u}^{v^k}). \qquad (14)$$

2. Find

$$\{\mathbf{u}^{h^{k+1}}, \mathbf{u}^{v^{k+1}}\} =$$
$$\operatorname{argmin}_{\{\mathbf{u}^h, \mathbf{u}^v\}} \tilde{\mathcal{M}}(\mathbf{q}^k(\mathbf{y}), \mathbf{Y}, \mathbf{x}, \mathbf{u}^h, \mathbf{u}^v). \qquad (15)$$

Set $\mathbf{q}(\mathbf{y}) = \lim_{k\to\infty} \mathbf{q}^k(\mathbf{y})$.

To calculate $\{\mathbf{u}^{h^{k+1}}, \mathbf{u}^{v^{k+1}}\}$, for $b = 1, \ldots, B$, in Eq. (15) we have that (see Eq. 12)

$$\mathbf{u}_b^{h^{k+1}} = \arg\min_{\mathbf{u}_b^h} \sum_{i=1}^P \frac{\mathbf{E}_{\mathbf{q}^k(\mathbf{y})}\left[(\Delta_i^h(\mathbf{y}_b))^2\right] + \mathbf{u}_b^h(i)}{\sqrt{\mathbf{u}_b^h(i)}},$$

and

$$\mathbf{u}_b^{v^{k+1}} = \arg\min_{\mathbf{u}_b^v} \sum_{i=1}^P \frac{\mathbf{E}_{\mathbf{q}^k(\mathbf{y})}\left[(\Delta_i^v(\mathbf{y}_b))^2\right] + \mathbf{u}_b^v(i)}{\sqrt{\mathbf{u}_b^v(i)}},$$

and consequently

$$\mathbf{u}_b^{h^{k+1}}(i) = \mathbf{E}_{\mathbf{q}^k(\mathbf{y})}\left[\Delta_i^h(\mathbf{y}_b))^2\right], \qquad (16)$$

and

$$\mathbf{u}_b^{v^{k+1}}(i) = \mathbf{E}_{\mathbf{q}^k(\mathbf{y})}\left[\Delta_i^v(\mathbf{y}_b))^2\right], \qquad (17)$$

for $i = 1, \ldots, p$ and $b = 1, \ldots, B$.

It is clear from Eqs. (16) and (17) that the vectors $\mathbf{u}_b^{h^{k+1}}$ and $\mathbf{u}_b^{v^{k+1}}$ are, respectively, functions of the spatial first order horizontal and vertical differences of the

unknown image $\mathbf{y}$ under the distribution $\mathbf{q}^k(\mathbf{y})$ and represent the local spatial activity of $\mathbf{y}$. This means that for pixels in zones with low local spatial activity, the values of $\mathbf{u}_b^h(i)$ and $\mathbf{u}_b^v(i)$ will be small and, hence, the quadratic term in Eq. (12) will keep the region smooth, controlling any noise amplification. However, for pixels in regions with high spatial activity such as edges or highly detailed zones, $\mathbf{u}_b^h(i)$ or $\mathbf{u}_b^v(i)$, or both, will be high thus preventing the prior model to smooth the edge or the details.

To calculate $\mathbf{q}^k(\mathbf{y})$, we observe that differentiating the integral on the right-hand side of Eq. (14) with respect to $\mathbf{q}(\mathbf{y})$ and setting it equal to zero, we obtain that

$$\mathbf{q}^k(\mathbf{y}) = \mathcal{N}\left(\mathbf{y} \mid \mathbf{E}_{q^k(\mathbf{y})}[\mathbf{y}], \mathbf{cov}_{q^k(\mathbf{y})}[\mathbf{y}]\right),$$

with

$$\mathbf{cov}_{q^k(\mathbf{y})}[\mathbf{y}] = \mathcal{A}^{-1}(\mathbf{u}^{h^k}, \mathbf{u}^{v^k}),$$

and

$$\mathbf{E}_{q^k(\mathbf{y})}[\mathbf{y}] = \mathbf{cov}_{q^k(\mathbf{y})}[\mathbf{y}]\phi^k,$$

where ϕ^k is the $(B \times p) \times 1$ vector

$$\phi^k = \left(\operatorname{diag}(\beta) \otimes \mathbf{H}^t\right)\mathbf{Y} + \gamma(\lambda \otimes \mathbf{x}),$$

where $\otimes$ is the Kronecker product, $\beta = (\beta_1, \beta_2, \ldots, \beta_B)^t$, $\lambda = (\lambda_1, \lambda_2, \ldots, \lambda_B)^t$, and

$$\mathcal{A}(\mathbf{u}^{h^k}, \mathbf{u}^{v^k}) = \operatorname{diag}(\beta) \otimes \mathbf{H}^t\mathbf{H} + \gamma(\lambda\lambda^t) \otimes \mathbf{I}_p$$
$$+ \begin{pmatrix} \mathcal{G}(\mathbf{u}_1^{h^k}, \mathbf{u}_1^{v^k}) & \mathbf{0}_p & \cdots & \mathbf{0}_p \\ \mathbf{0}_p & \mathcal{G}(\mathbf{u}_2^{h^k}, \mathbf{u}_2^{v^k}) & \cdots & \mathbf{0}_p \\ \vdots & \vdots & \ddots & \vdots \\ \mathbf{0}_p & \mathbf{0}_p & \cdots & \mathcal{G}(\mathbf{u}_B^{h^k}, \mathbf{u}_B^{v^k}) \end{pmatrix}$$
$$+ \begin{pmatrix} \sum_{b=1}^B \mu_{1b} & -\mu_{12} & \cdots & -\mu_{1B} \\ -\mu_{21} & \sum_{b=1}^B \mu_{2b} & \cdots & -\mu_{2B} \\ \vdots & \vdots & \ddots & \vdots \\ -\mu_{B1} & -\mu_{B2} & \cdots & \sum_{b=1}^B \mu_{Bb} \end{pmatrix} \otimes \mathbf{I}_p,$$

where $\mu_{bb} = 0$, $\forall b$, $\mu_{bb'} = \nu_{bb'}, b' > b$ and $\mu_{b'b} = \mu_{bb'}$,

$$\mathcal{G}(\mathbf{u}_b^{h^k}, \mathbf{u}_b^{v^k}) = \alpha_b^h \Delta^{h^t} W(\mathbf{u}_b^{h^k})\Delta^h + \alpha_b^v \Delta^{v^t} W(\mathbf{u}_b^{v^k})\Delta^v,$$

for $b = 1, \ldots, B$, where Δ^h and Δ^v represent $p \times p$ convolution matrices associated with the first order horizontal and vertical differences, respectively, and $W(\mathbf{u}_b^{h^k})$ and $W(\mathbf{u}_b^{v^k})$ are $p \times p$ diagonal matrices of the form $W(\mathbf{u}_b^{d^k}) = \operatorname{diag}\left(\mathbf{u}_b^{d^k}(i)^{-\frac{1}{2}}\right)$, for $i = 1, \ldots, p$, $d = h, v$. These matrices can be interpreted as spatial adaptivity matrices since they control the amount of smoothing at each pixel location depending on the strength of the intensity variation at that pixel, as expressed by the horizontal and vertical intensity gradients, respectively.

That is, for pixels with high spatial activity in the horizontal (vertical) direction, the corresponding entries of $W(\mathbf{u}_b^{h^k})$ $(W(\mathbf{u}_b^{v^k}))$ are very small, which means that no smoothness is enforced in this direction, while for areas where pixels have similar values in the horizontal or vertical direction the corresponding entries of $W(\mathbf{u}_b^{h^k})$ or $W(\mathbf{u}_b^{v^k})$, respectively, are very large, which means that smoothness is enforced in the corresponding direction.

4 Experimental Results

In order to assess the quality of the proposed approach, we report results on a synthetic color image, that helps us illustrate the usefulness of the term that takes into account the correlation between image bands in the prior model (see Eq. (4)), and a Landsat ETM+ and a IKONOS multispectral images.

The proposed method, that we name $\ell 1cor$, is compared with the method without considering the correlation between the bands (henceforth $\ell 1$), obtained by setting $\nu_{b,b'} = 0$, $\forall b, b' = 1, \ldots, B$. Also we compare it with the Bayesian method in [11] (henceforth SAR), which utilizes a simultaneous auto-regressive prior model, bicubic interpolation (henceforth BIC), the IHS method in [5], and the additive wavelet pansharpening method (AWL) in [12]. In addition, results for the method in [14] (henceforth PRI) are reported when a downsampling factor of two is used.

To assess numerically the quality of the reconstructed multispectral images both spatial and spectral measures have to be considered. Spatial improvement was assessed by means of the correlation of the high frequency components (COR) [17] which measures the spatial similarity between each reconstructed multispectral image band and the panchromatic image. The COR index takes values between 0 and 1 (the higher the value the better the quality of the reconstruction). Spectral fidelity was assessed by means of the peak signal-to-noise ratio (PSNR) and structural similarity (SSIM) index [19], a perceptual quality measure that takes into account the luminance, contrast and structure differences, between each band of the reconstructed and original multispectral images. The SSIM index takes values between -1 and 1. The closer the SSIM index to one the better the reconstruction, with 1 only being reachable when the two images are identical. The mean value for COR, PSNR and SSIM act as global fidelity measures for the reconstructed multispectral image, as well as the standard ERGAS (from the French Erreur Relative Globale Adimensionalle de Synthése) index [18], a dimensionless global criterion which considers the ratio of the root mean squared error (RMSE) and the band-

wise mean. The lower the value of this index, especially a value lower than the number of bands B, the higher the quality of the multispectral image.

Our first experiment was conducted on the 120×120 color image whose detail is displayed in Fig. 2(a). Following [1], we simulate the spatially degraded data using the Modulation Transfer Function (MTF) of the satellite imaging system. This MTF "is generally bell shaped, and its magnitude value at the cutoff Nyquist frequency is far lower than 0.5, to prevent aliasing. . . . As a tradeoff between maximum spatial resolution and minimum aliasing of the sampled signal, the Nyquist frequency is usually chosen such that the corresponding magnitude value is around 0.2" [1]. Hence, to obtain a low resolution color image, each band of the original image was first blurred using a Gaussian blur with a magnitude value of 0.2 at Nyquist frequency, that simulate the MTF of the satellite, and then downsampled by a factor of two by discarding every other pixel in each direction. Finally, zero mean Gaussian noise was added to each band to obtain two observed multispectral images with a signal-to-noise ratio (SNR) of 20 dB and 30 dB. The panchromatic image was obtained from the original high resolution color image using the model in Eq. (7), with $\lambda = [0.3, 0.6, 0.1]^t$, and adding zero mean Gaussian noise with an SNR of 20 dB and 30 dB. Details of the 30 dB observed multispectral and panchromatic images are depicted in Figs. 2(b) and 2(c), respectively.

We run the proposed algorithm until the criterion $\|\mathbf{E}_{q^k(\mathbf{y})}[\mathbf{y}] - \mathbf{E}_{q^{k-1}(\mathbf{y})}[\mathbf{y}]\|^2 / \|\mathbf{E}_{q^{k-1}(\mathbf{y})}[\mathbf{y}]\|^2 < 5 \ 10^{-4}$ was satisfied. The values of the noise parameters are known to be $\beta = (0.053, 0.061, 0.07)^t$ and $\gamma = 0.053$ for the 20dB SNR image. The values for α_d, $d = h, v$, are determined as $\alpha_d = C_\alpha / \sum_{i=1}^{P} \|\Delta_i^d(\mathbf{Y}_b))\|^2$, where C_α was manually selected to maximize the mean PSNR of the reconstruction. Once these values are fixed, the values for $\nu_{i,j}$ are determined as $\nu_{i,j} = C_\nu / \|\mathbf{Y}_i - \mathbf{Y}_j\|^2$, where C_ν was manually selected to maximize the mean PSNR of the obtained reconstruction. Following this procedure we obtained $\alpha^h = (3.9, 3.9, 3.8)^t \times 10^{-2}$, $\alpha^v = (3.2, 3.2, 3.1)^t \times 10^{-2}$, and $\nu = (\nu_{1,2}, \nu_{1,3}, \nu_{2,3}) = (55, 9.8, 24) \times 10^{-4}$. For the 30dB SNR image the noise parameter are known to be $\beta = (0.53, 0.61, 0.73)^t$ and $\gamma = 0.53$, and the other parameters were $\alpha^h = (3.9, 3.9, 3.8)^t \times 10^{-3}$, $\alpha^v = (3.2, 3.2, 3.1)^t \times 10^{-3}$, and $\nu = (\nu_{1,2}, \nu_{1,3}, \nu_{2,3}) = (55, 8.1, 20) \times 10^{-4}$.

Figure 2 displays the resulting images for the proposed method as well as the methods we are comparing against. From the images it is clear that the proposed method (Fig. 2(i)) obtains sharper edges than the method in [11], with more detailed elements (observe, for example, the fence and the banister above it) and achieves higher similarity to the colors of the orig-
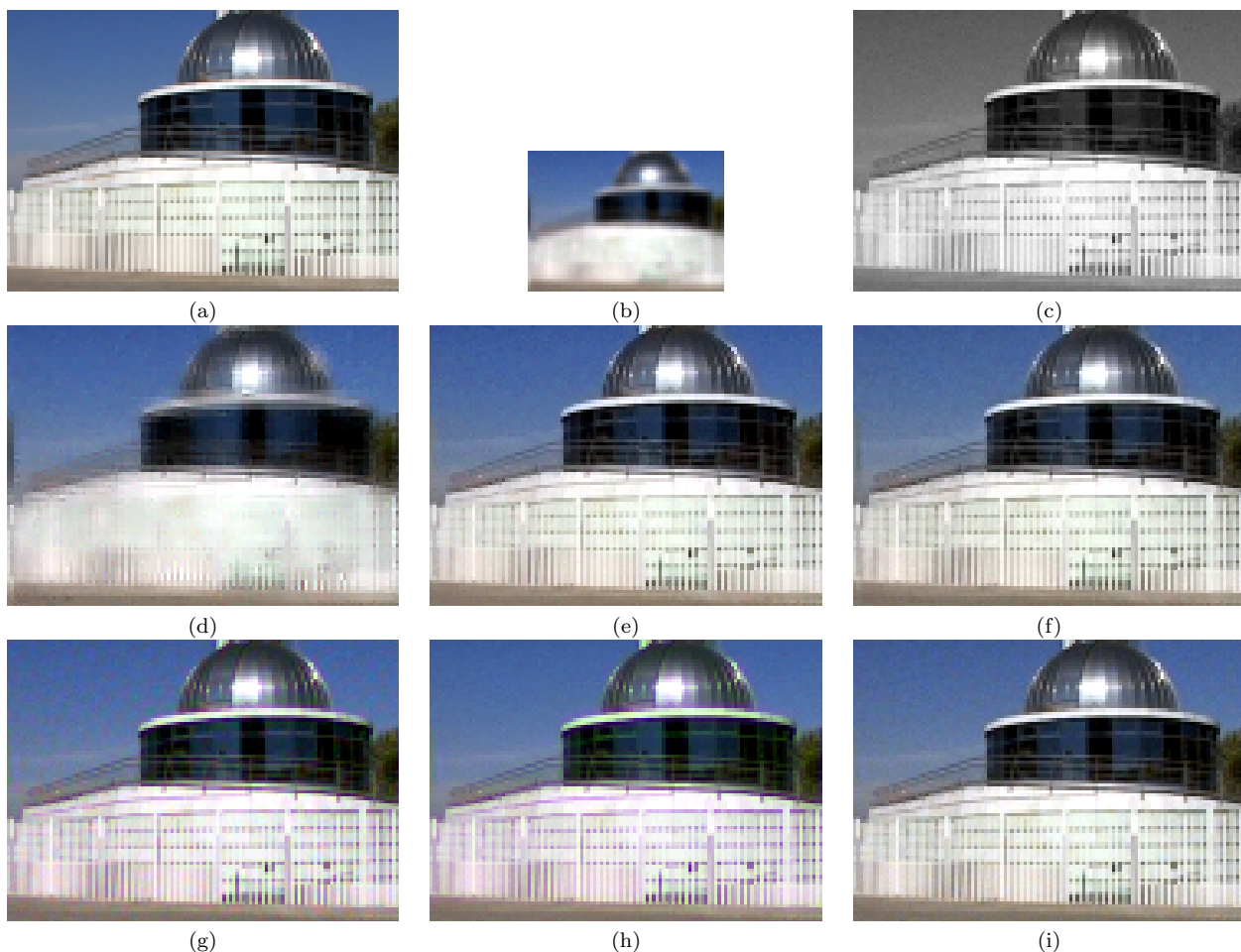
Fig. 2 (a) Original RGB image; (b) Observed LR multispectral image; (c) Observed panchromatic image; (d) Reconstruction using PRI; (e) Reconstruction using IHS; (f) Reconstruction using AWL; (g) Reconstruction using SAR; (h) Reconstruction using $\ell 1$; (i) Reconstruction using $\ell 1$cor.

Fig. 3 Representation of $\mathbf{u}_b^{d-\frac{1}{2}}$, for $b = 1, 2, 3$ represented as R, G and B bands, respectively, of the image displayed in Fig. 2, a) for $d = h$, b) for $d = v$.

inal image than the $\ell 1$ method, reducing the greenish appearance of the white strip under the dome and the color bleeding in the fence. The results are visually very similar to IHS and AWL although a detailed inspection can show that the proposed method reduced a bit more the noise in the image.

Numerical results, presented in Table 1, also support the use of the proposed model. Its figures of merit are, in general, better than the ones provided by all other methods except for the band 3 of the 20 dB SNR image where the COR and PSNR values are smaller than the ones obtained by the IHS and AWL. The high values for IHS and AWL were expected since the panchromatic image is a perfect realization of the intensity band of IHS transform. Note however that the proposed method provides a much better reconstruction for bands 1 and 2 and better SSIM for all the bands and a much lower ERGAS value and better mean values. For the image with 30dB SNR the method provides the best results, increasing all the quality indices and obtaining a lower ERGAS. It is interesting to see how the proposed method increases the quality of the results over the $\ell 1$ method, which clearly demonstrates the benefits of introducing the correlation between the multispectral image bands.

Figure 3 depicts the value of $\mathbf{u}_b^h(i)^{-\frac{1}{2}}$ and $\mathbf{u}_b^v(i)^{-\frac{1}{2}}$, $b = 1, 2, 3$, at convergence of the algorithm for the image in Fig. 2(i). In the figure, the spatial adaptivity values for band 1 are represented in red, the values for band

Table 1 Values of PSNR, COR and SSIM for the different bands and in mean, and ERGAS value for the synthetic color image.

SNR	Method	PSNR 1	2	3	mean	COR 1	2	3	mean	SSIM 1	2	3	mean	ERGAS
20 dB	BIC	25.4	25.5	25.5	25.5	0.39	0.40	0.40	0.40	0.63	0.64	0.64	0.64	6.84
	PRI	26.2	26.4	26.2	26.2	0.63	0.65	0.64	0.63	0.63	0.64	0.66	0.64	6.24
	IHS	31.5	31.9	31.3	31.3	0.98	0.98	0.97	0.98	0.86	0.86	0.86	0.86	3.38
	AWL	31.6	32.3	31.6	31.5	0.99	0.99	0.99	0.99	0.85	0.86	0.86	0.86	3.28
	SAR	30.3	34.0	27.4	30.6	0.92	0.99	0.63	0.85	0.82	0.89	0.71	0.81	4.04
	ℓ1	30.9	33.8	27.5	30,7	0.88	0.96	0.60	0,81	0.86	0.92	0.75	0.84	3.95
	ℓ1cor	32.7	37.1	30.7	33.5	0.99	0.97	0.88	0.95	0.92	0.96	0.89	0.92	2.88
30 dB	BIC	25.7	25.7	25.7	25.7	0.43	0.44	0.43	0.43	0.68	0.68	0.68	0.68	6.65
	PRI	27.1	27.1	26.9	27.0	0.73	0.73	0.71	0.72	0.75	0.76	0.76	0.76	5.69
	IHS	34.5	35.0	33.7	34.4	0.99	0.99	0.98	0.99	0.96	0.97	0.96	0.96	2.44
	AWL	35.8	37.1	34.9	35.9	1.00	1.00	0.99	1.00	0.97	0.98	0.97	0.97	2.06
	SAR	33.5	36.7	28.9	33.0	0.97	1.00	0.71	0.89	0.91	0.96	0.79	0.89	3.15
	ℓ1	34.4	35.9	28.3	32.9	0.98	0.99	0.71	0.89	0.95	0.97	0.81	0.91	3.25
	ℓ1cor	40.0	43.6	37.0	40.2	1.00	1.00	0.99	1.00	0.98	0.98	0.95	0.97	1.34

2 are represented in green and for band 3, in blue. For a better visualization, the images have been contrast stretched so that a total of 1% of the values are saturated at low and high intensities. Notice that the main features in the image are represented in the images with lower values of $\mathbf{u}_b^d(i)^{-\frac{1}{2}}$, $d = \{h, v\}$, and that the same features are detected in most of the bands.

In a second experiment, the method was tested on a real Landsat ETM+ image. Figure 4(a) depicts a 128×128 RGB color region of interest composed of bands 3, 2, and 1 of a Landsat ETM+ multispectral image. According to the ETM+ sensor spectral response (see Fig. 1), the panchromatic image covers only the spectrum of part of the first four bands of the multispectral image although the sensor sensibility is not constant over the whole range. Hence, we apply the proposed method with $B = 4$. The values of λ_b, $b = 1, 2, 3, 4$, were calculated from the spectral response of the ETM+ sensor, by summing up the spectral response of the panchromatic sensor weighted by the response of the sensor for each multispectral band. The obtained values were then normalized so that their sum equals one, thus producing values equal to 0.0078, 0.242, 0.2239, and 0.5263, for bands one to four, respectively.

Note that in this experiment we do not have access to the original high resolution multispectral image to numerically evaluate the quality of the different reconstructions. In order to obtain a numerical comparison and to overcome the lack of an exact HR multispectral image to compare with, an intermediate step has been performed in which a simulated multispectral image of size 64×64 pixels, whose RGB channels are shown in Fig. 4(b), was obtained from the observed 128×128 pixels multispectral image by applying a Gaussian MTF blur with a 0.2 magnitude value at Nyquist frequency, and downsampling the resulting image by a factor of two in each direction. The panchromatic observation of

size 128×128 pixels, shown in Fig. 4(c), was also generated using the model in Eq. (7) with $\lambda_1 = 0.0078$, $\lambda_2 = 0.242$, $\lambda_3 = 0.2239$, and $\lambda_4 = 0.5263$.

The proposed algorithm was run until convergence using the noise parameter values $\beta = (3.0, 4.0, 5.1, 2.9)^t$ and $\gamma = 3.48$. We selected these low noise values, because the results are compared with the originally observed image which, to the effects of this experiment, are considered noiseless. The rest of the parameters were experimentally determined to have the following values $\alpha^h = (3.5, 3, 4, 2.2, 1.6)^t \times 10^{-2}$, $\alpha^v = (3.7, 3.5, 2.4, 1.6)^t \times 10^{-2}$, and $\nu = (\nu_{1,2}, \nu_{1,3}, \nu_{1,4}, \nu_{2,3}, \nu_{2,4}, \nu_{3,4})^t = (5, 2, 4, 13, 2, 1)^t \times 10^{-6}$.

A numerical comparison between the different 128×128 reconstructions and the observed 128×128 multispectral image is presented in Table 2. The reconstructed RGB color images are displayed in Fig. 4. The images show that PRI (Fig. 4(d)) produced a blurred image, IHS (Fig. 4(e)) and AWL (Fig. 4(f)) introduced a high amount of details (see the high COR values in Table 2) but also introduced a high chromatic distortion and SAR (Fig. 4(g)) smoothed out sharp edges. The $\ell1$ method (Fig. 4(h)) produced crisper edges but did not reconstruct well the colors near some edges. However, the proposed method (Fig. 4(i)) successfully included the details of the panchromatic image, producing sharp edges and maintaining the small details while preserving the spectral quality of the image.

Finally, in a third experiment, we used the IKONOS multispectral image of size 128×128, whose bands 3, 2 and 1 (R,G, and B, respectively) are depicted in Fig. 5(a), and bands 4, 3 and 2, utilizing false RGB colors, in Fig. 6(a). As in the previous experiment, a low resolution multispectral image was obtained (see Figs. 5(b) and 6(b)) by blurring the original multispectral image with a Gaussian MTF blur with a magnitude value of 0.28 at Nyquist frequency, which is a magnitude
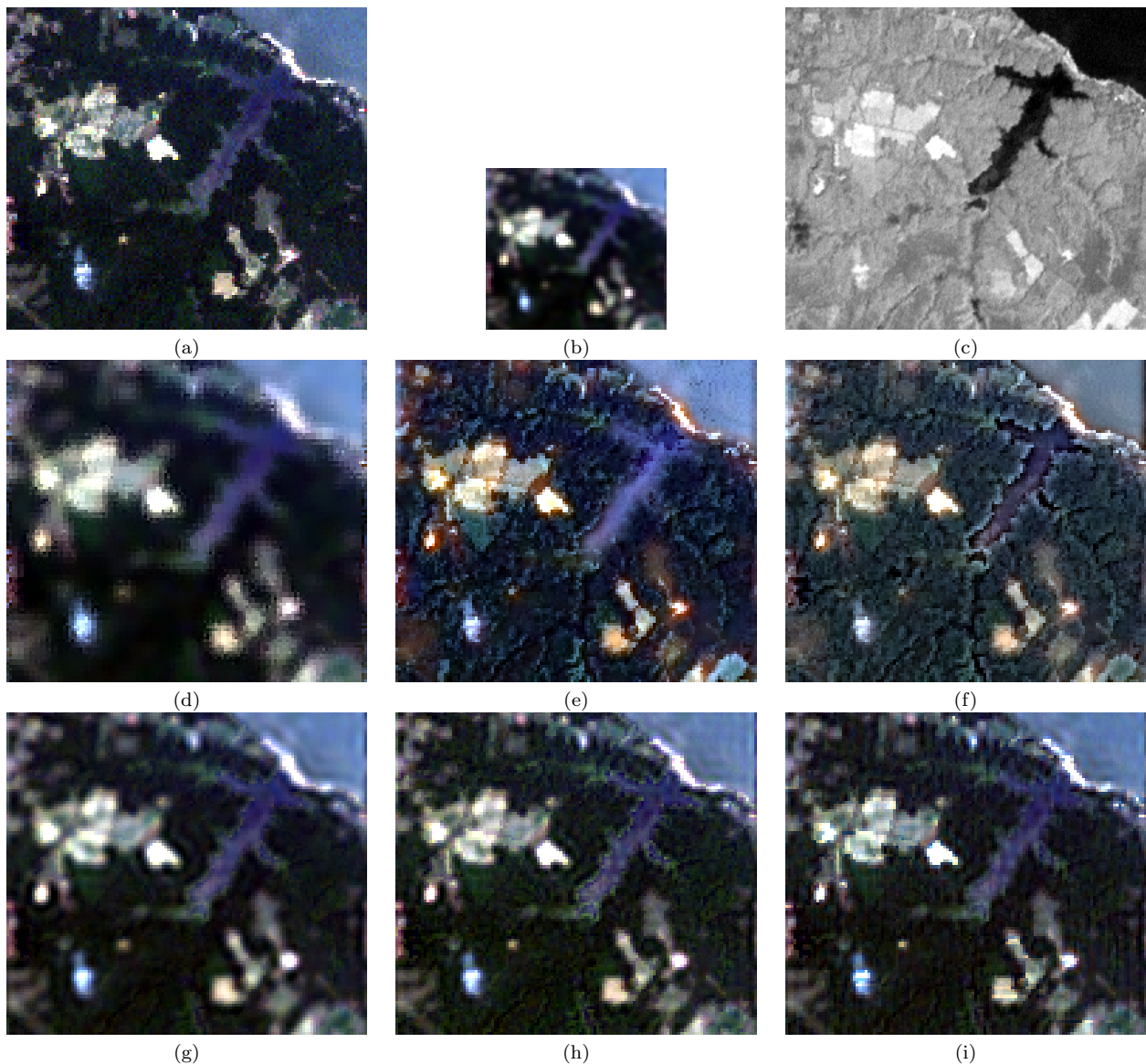
Fig. 4 (a) Original RGB Landsat multispectral image; (b) Observed LR multispectral image; (c) Observed panchromatic image; (d) Reconstruction using PRI; (e) Reconstruction using IHS; (f) Reconstruction using AWL; (g) Reconstruction using SAR; (h) Reconstruction using $\ell 1$; (i) Reconstruction using the proposed $\ell 1$cor method.

value consistent with the IKONOS multispectral sensor technical characteristics (see [6]), and then down-sampling it by a factor of four in each direction. The panchromatic image (Fig. 5(c)) was generated using the model in Eq. (7) with $\lambda_1 = 0.1071$, $\lambda_2 = 0.2646$, $\lambda_3 = 0.2696$, and $\lambda_4 = 0.3587$.

The proposed algorithm was run until convergence with the parameter values $\beta = (0.90, 0.82, 1.10, 0.47)^t$, $\gamma = 0.69$, $\alpha^h = (1, 5, 1.0, 0.9, 0.4)^t \times 10^{-3}$, $\alpha^v = (1, 6, 1.0, 1.0, 0.4)^t \times 10^{-3}$ and $\nu = (30, 10, 0.3, 5, 0.4, 0.25) \times 10^{-6}$. A numerical comparison between the different reconstructions and the observed multispectral image is presented in Table 3. The reconstructions obtained applying the different methods to bands 3, 2 and 1 (RGB)

are depicted in Fig. 5, and in Fig. 6 for bands 4, 3 and 2, utilizing false RGB colors. The numerical comparison between the different methods favors the three Bayesian Methods, which obtain much better PSNR and SSIM values than the IHS and AWL with a similar COR value. $\ell 1$ gives results better than SAR, and the introduction of the correlations between bands in the proposed method $\ell 1$cor is more relevant for the bands with a minor weight in the panchromatic, that is the blue band. The visual comparison of the images shown in Figs. 5 and 6 reveals the same progression, as the numerical one, between the three Bayesian methods. The two images corresponding to the AWL method, Figs. 5(f) and 6(f) are rich in details but, like the cor-

Table 2 Values of PSNR, COR and SSIM for the different bands and in mean, and ERGAS value for the Landsat image in Fig. 4.

Method	PSNR					COR					SSIM					ERGAS
	1	2	3	4	mean	1	2	3	4	mean	1	2	3	4	mean	
BIC	39.7	37.3	33.1	30.9	35.2	0.83	0.83	0.82	0.85	0.83	0.93	0.91	0.86	0.79	0.88	3.81
PRI	39.8	37.8	33.7	31.7	35.7	0.84	0.85	0.80	0.88	0.84	0.93	0.92	0.87	0.84	0.89	3.55
IHS	37.3	37.1	33.6	32.5	35.8	0.94	0.95	0.95	0.95	0.95	0.91	0.92	0.87	0.89	0.90	3.60
AWL	35.4	36.1	33.6	35.4	35.1	0.99	0.99	0.97	0.99	0.98	0.86	0.89	0.85	0.93	0.88	3.56
SAR	41.3	40.5	36.8	40.1	39.7	0.84	0.90	0.92	0.98	0.91	0.95	0.95	0.93	0.97	0.95	2.27
$\ell 1$	41.6	41.7	38.1	41.4	40.7	0.84	0.90	0.90	0.97	0.90	0.95	0.96	0.94	0.97	0.96	1.98
$\ell 1$cor	41.7	41.9	37.9	41.4	40.7	0.85	0.91	0.91	0.98	0.91	0.95	0.96	0.94	0.97	0.95	2.00

(a)   (b)
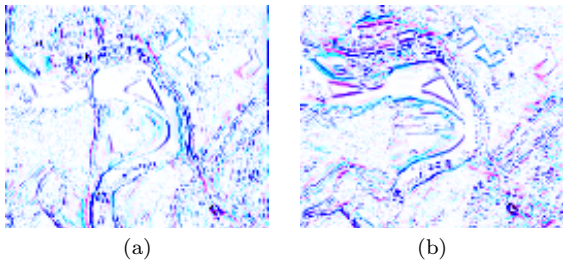
Fig. 7 Representation of $\mathbf{u}_b^{d-\frac{1}{2}}$, for $b = 1, 2, 3$ represented as R, G and B bands, respectively, of the image displayed in Fig. 2, a) for $d = h$, b) for $d = v$.

responding to the IHS method images in Figs. 5(e) and 6(e), exhibit color distortions not present in the three Bayesian methods Figs. 5(h–j) and 6(h–j). These color distortions are more appreciable in the images corresponding to the visible spectrum of Fig. 5 than in the green, red and near-infrared ones of Fig. 6. The quality improvement with respect to the previous methods have, however, a cost in computational burden. While BIC, PRI, IHS and AWL methods take less than a second, the proposed method took around 24 seconds to reconstruct the image, a time similar to the needed by $\ell 1$ and less than the time needed by the SAR method.

Figure 7 depicts the spatial activity factors for the proposed method for the image shown in Fig. 5(j). In the figure, the spatial adaptivity values for band 3 are represented in red, the values for band 2 are represented in green and the values for band 1 are represented in blue. The method captures the structure of the image, assigning a lower value of $\mathbf{u}_b^h(i)$ or $\mathbf{u}_b^v(i)$ to the edges of the objects, although in this case the images present more different colors meaning that some features present in some bands did not appear or appear with much less strength in other bands.

5 Conclusions

We have presented a new method for the pansharpening of multispectral images using a super resolution approach which takes into account the sensor characteristics in the image formation model and incorporates prior knowledge on the expected characteristics of multispectral images by imposing smoothness within each band and by taking into account the correlation among pixels in the same position in different bands of the multispectral image. This correlation is, to the best of our knowledge, the first time that it is explicitly used in pansharpening. We have used the variational approach to approximate the posterior distribution of the pansharpened multispectral image. Based on the presented experimental results, the proposed method successfully incorporates the high frequencies of the panchromatic image into the reconstructed image while preserving the spectral quality of the image.

References

1. B. Aiazzi, L. Alparone, S. Baronti, A. Garzelli, and M. Selva. MTF-tailored multiscale fusion of high-resolution MS and Pan imagery. *Phot. Eng. & Rem. Sens.*, 72(5):591–596, 2006.
2. B. Aiazzi, L. Alparone, S. Baronti, I. Pippi, and M. Selva. Generalised Laplacian pyramid-based fusion of MS + P image data with spectral distortion minimisation. *ISPRS Internat. Archives Photogramm. Remote Sensing*, 34:3–6, 2002.
3. L. Alparone, L. Wald, J. Chanussot, C. Thomas, P. Gamba, and L.M. Bruce. Comparison of pansharpening algorithms: Outcome of the 2006 GRS-S data-fusion contest. *IEEE Trans. on Geosc. & Rem. Sens.*, 45(10):3012–3020, 2007.
4. J. Bioucas-Dias, M. Figueiredo, and J. Oliveira. Total-variation image deconvolution: A majorization-minimization approach. In *Proc. of the 2006 Int. Conf. on Acoustics, Speech and Signal Processing (ICASSP'2006)*, volume 2, pages II–861–II–864, 2006.
5. W. J. Carper, T. M. Lillesand, and R. W. Kiefer. The use of intensity-hue-saturation transformations for merging SPOT panchromatic and multispectral image data. *Phot. Eng. & Rem. Sens.*, 56(4):459–467, 1990.
6. M.K. Cook, B.A. Peterson, G. Dial, L. Gibson, F.W. Gerlach, K.S. Hutchins, R. Kudola, and H.S. Bowen. IKONOS technical performance assessment. *Proc. SPIE*, 4381:94–108, 2001.
7. M.M. Khan, L. Alparone, and J. Chanussot. Pansharpening quality assessment using the modulation transfer functions of instruments. *IEEE Transactions on Geoscience and Remote Sensing*, 47(11):3880–3891, 2009.
8. S. Kullback and R. A. Leibler. On information and sufficiency. *Annals of Math. Stat.*, 22:79–86, 1951.
9. K. Lange. Optimization. In *Springer texts in Statistic*. New York, Springer Verlag, 2004.
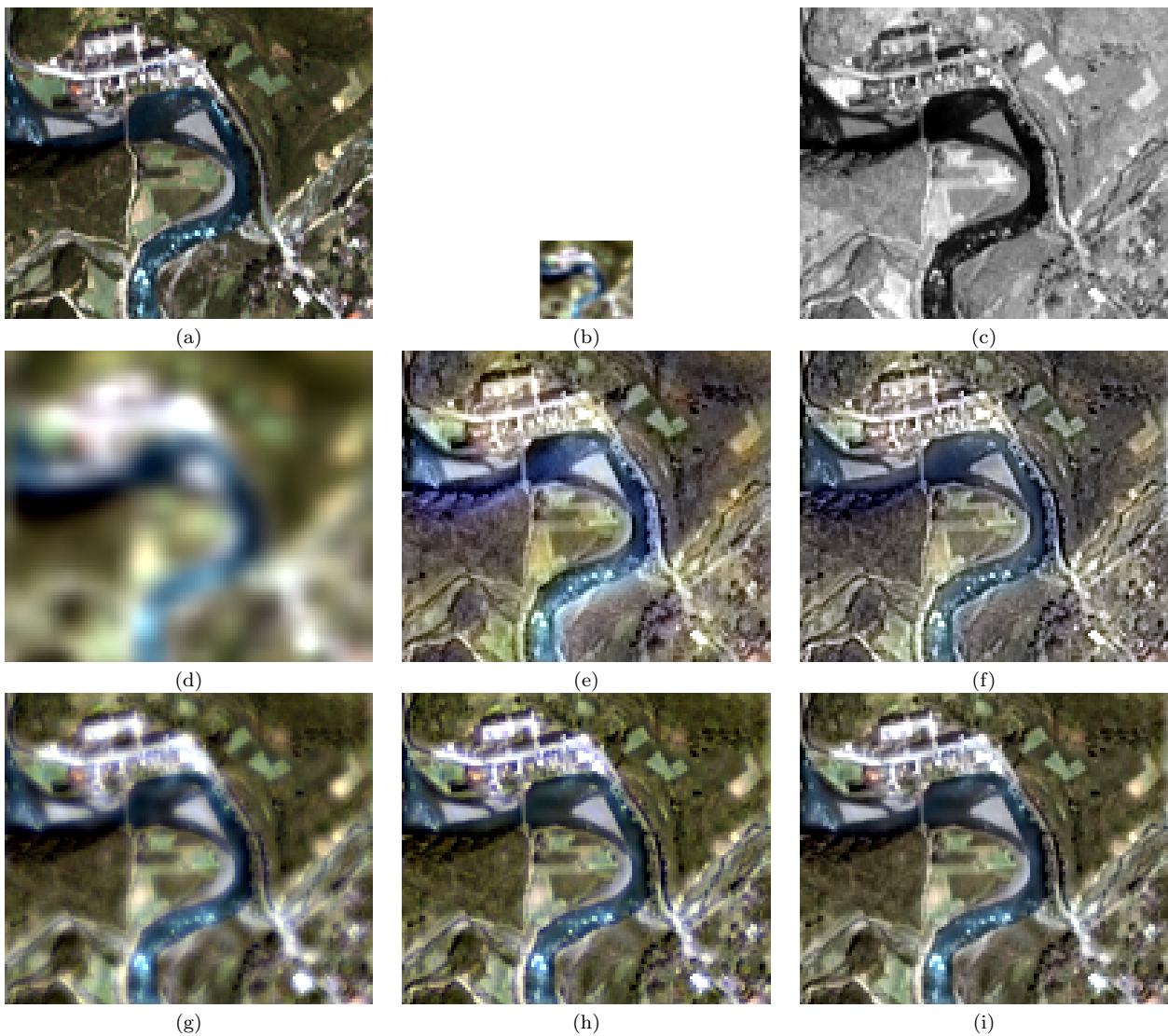
Fig. 5 (a) Original RGB IKONOS multispectral image; (b) Observed LR multispectral image; (c) Observed panchromatic image; (d) Reconstruction using BIC; (e) Reconstruction using IHS; (f) Reconstruction using AWL; (g) Reconstruction using SAR; (h) Reconstruction using $\ell 1$; (i) Reconstruction using the proposed $\ell 1$cor method.

10. M. Lillo-Saavedra and C. Gonzalo. Multispectral images fusion by a joint multidirectional and multiresolution representation. *International Journal of Remote Sensing*, 28(18):4065–4079, 2007.

11. R. Molina, M. Vega, J. Mateos, and A.K. Katsaggelos. Variational posterior distribution approximation in Bayesian super resolution reconstruction of multispectral images. *Applied and Computat. Harmonic Analysis*, 24(2):251–267, 2008.

12. J. Nuñez, X. Otazu, O. Fors, A. Prades, V. Pala, and R. Arbiol. Multiresolution-based image fusion with additive wavelet decomposition. *IEEE Trans on Geosc. & Rem. Sens.*, 37(3):1204–1211, 1999.

13. X. Otazu, M. Gonzalez-Audicana, O. Fors, and J. Nuñez. Introduction of sensor spectral response into image fusion methods. application to wavelet-based methods. *IEEE Trans on Geosc. & Rem. Sens.*, 43(10):2376–2385, 2005.

14. J.C. Price. Combining multispectral data of different spatial resolution. *IEEE Trans. on Geosc. & Rem. Sens.*, 37(3):1199–1203, 1999.

15. V. P. Shah, N. H. Younan, and R. L. King. An efficient pansharpening method via a combined adaptive pca approach and contourlets. *IEEE Transactions on Geoscience and Remote Sensing*, 46(5):1323–1335, 2008.

16. M. Vega, R. Molina, and A.K. Katsaggelos. L1 prior majorization in Bayesian image restoration. In *16th Int. Conf. on Digital Signal Processing*, 2009.

17. V. Vijayaraj. A quantitative analysis of pansharpened images. Master's thesis, Mississippi St. University, 2004.

18. L. Wald, T. Ranchin, and M. Mangolini. Fusion of satellite images of different spatial resolutions: assessing the quality of resulting images. *Phot. Eng. Rem. Sens.*, 63(6):691–699, 1997.

19. Z. Wang, A. C. Bovik, H. R. Sheikh, and E. P. Simoncelli. Image quality assessment: From error visibility to structural similarity. *IEEE Trans. on Img Proc.*, 13(4):600–612, 2004.
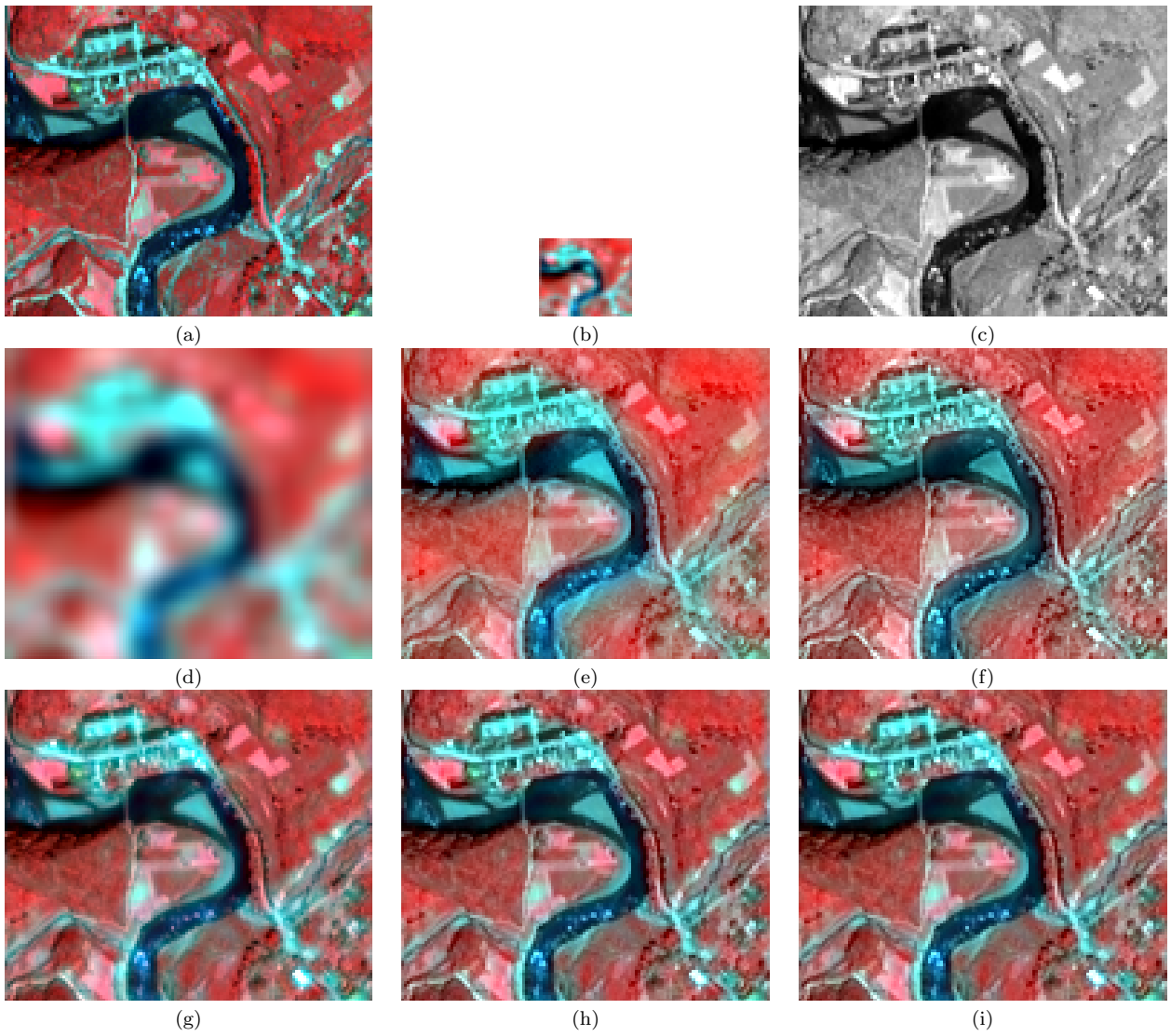
Fig. 6 (a) Original NIRRG IKONOS multispectral image; (b) Observed LR multispectral image; (c) Observed panchromatic image; (d) Reconstruction using the PRI; (e) Reconstruction using IHS; (f) Reconstruction using AWL; (g) Reconstruction using SAR; (h) Reconstruction using $\ell 1$; (i) Reconstruction using the proposed $\ell 1cor$ method.

Table 3 Values of PSNR, COR and SSIM for the different bands and in mean, and ERGAS values for the IKONOS image in Fig. 5.

Method	PSNR					COR					SSIM					ERGAS
	1	2	3	4	mean	1	2	3	4	mean	1	2	3	4	mean	
BIC	17.6	14.1	13.6	7.6	13.2	0.65	0.65	0.64	0.65	0.65	0.35	0.25	0.24	0.21	0.26	9.05
IHS	17.4	15.5	14.9	9.2	14.2	0.97	0.96	0.98	0.87	0.94	0.53	0.58	0.52	0.49	0.53	7.83
AWL	17.8	16.7	15.8	9.6	15.0	0.99	0.99	0.97	0.97	0.98	0.51	0.62	0.56	0.61	0.57	7.20
SAR	20.5	18.9	18.3	14.0	17.9	0.73	0.93	0.96	0.98	0.90	0.60	0.70	0.67	0.84	0.70	5.13
$\ell 1$	21.7	19.6	18.7	14.8	18.7	0.83	0.99	0.97	0.99	0.94	0.67	0.72	0.67	0.83	0.72	4.76
$\ell 1cor$	22.3	19.8	18.7	14.8	18.9	0.93	0.99	0.98	0.99	0.97	0.68	0.72	0.67	0.83	0.72	4.68